The Meteoritical Society

Meteoritics & Planetary Science 55, Nr 11, 2404–2421 (2020)
doi: 10.1111/maps.13585

Biconical reflectance, micro-Raman, and nano-FTIR spectroscopy of the Didim (H3-5) meteorite: Chemical content and molecular variations

M. YESILTAS[1*], M. KAYA[2], T. D. GLOTCH[3], R. BRUNETTO[4], A. MATURILLI[5], J. HELBERT[5], and M. E. OZEL[6]

[1]Faculty of Aeronautics and Space Sciences, Kirklareli University, Kirklareli, 39100 Turkey
[2]Institute of Acceleration Technologies, Ankara University, Ankara, 06830 Turkey
[3]Department of Geosciences, Stony Brook University, Stony Brook, New York, 11794 USA
[4]Université Paris-Saclay, CNRS, Institut d'Astrophysique Spatiale, 91405 Orsay, France
[5]DLR, Berlin, Germany
[6]Space Sciences and Solar Energy Research and Application Center, Cukurova University, Adana, 01380 Turkey
*Corresponding author. E-mail: myesiltas@knights.ucf.edu

(Received 02 April 2020; revision accepted 23 September 2020)

Abstract–The Didim meteorite contains multiple lithologies and clasts of different petrologic types in a single stone. A mixture of H5 clasts in an unequilibrated H3 host was previously observed in Didim, according to the initial characterization reported in the Meteoritical Bulletin Database, providing an opportunity to investigate molecular composition that contains varying degree of equilibrium with varying mineralogy. We have taken a "from large scale to small scale" approach to spectroscopically investigate the chemical content of Didim. Centimeter-scale biconical reflectance spectra show that Didim contains abundant olivine, pyroxene, and other optically active minerals, evident from a strong Band I near 0.93 μm and a weak Band II near 1.75 μm. Micrometer-scale Raman spectroscopic investigations reveal the presence of carbonaceous material in addition to forsteritic olivine, pyroxene (augite and enstatite), feldspars, and opaque phases such as chromite and hematite. 3-D Raman tomographic imaging shows that the carbonaceous material near chondrules extends underneath a large olivine grain, going further down toward the interior, indicating that the observed carbonaceous matter is likely indigenous. Nano-scale infrared measurements reveal that the observed chemical materials in Didim contain spectral, and therefore, molecular, variations at the ~20 nm spatial scale. These chemical variations are normally not accessible via conventional infrared techniques, and indicate the presence of different cations in the molecular composition of observed minerals. By taking the "large scale to small scale" approach, we show that these compositional variations can be captured and investigated nondestructively in meteorites to understand formation/evolution of chemical components in the parent body.

INTRODUCTION

Meteorites originate mostly from asteroids, and the molecular compositions of these extraterrestrial samples play an important role for understanding the origin of their parent bodies and the alteration/thermal processes those bodies underwent. Ordinary chondrites constitute the majority of meteorites, and present a wide range of compositions and petrologic textures (Kallemeyn et al. 1989). While individual ordinary chondrites should present a uniform mineralogy across the sample, multiple lithologies with different mineralogical compositions are observed in some meteorites (e.g., McCoy et al. 1999; Kohout et al. 2010; Snape et al. 2011; Jenniskens et al. 2012). Compared to the rest of the ordinary chondrites, unequilibrated ordinary chondrites are petrologic type 3 chondrites with more primitive, less altered, and generally uniform chemical composition, forming a subgroup within the ordinary chondrites.

Didim fell in early February of 2007 in Didim, Turkey. Multiple stones were recovered from the fall area and some meteorite fragments were secured for research. Initial work on Didim showed that this meteorite contains multiple lithologies and clasts of different petrologic types even in a single stone (Weisberg et al. 2008). Namely, in addition to metal and sulfide phases, a mixture of H5 clasts in an unequilibrated H3 host was observed in Didim. Thus, it was classified as an H3-5 ordinary chondrite. Didim's complex chemistry provides an opportunity to investigate molecular compositions that contain varying degree of equilibrium with varying mineralogy. However, to our knowledge, no publication exists as of today about this meteorite and its chemical constituents.

Meteorites can contain multiple lithologies, which consist of chemically heterogeneous mineral compositions. Characterization of such lithologies and their content requires novel analytical techniques. High spatial resolution spectroscopic techniques such as Raman microspectroscopy (micro-Raman; Wang et al. 1999; Busemann et al. 2007; Fries and Steele 2008; Yesiltas et al. 2018, 2019, 2020) and Fourier transform infrared nanospectroscopy (nano-FTIR; Dominguez et al. 2014; Kebukawa et al. 2019) have the potential to reveal meteoritic organic and inorganic components in great detail via their active vibrational modes. Confocal Raman spectroscopy provides chemical mapping in two dimensions as well as three-dimensional tomographic imaging capability with micrometer resolution, while the nano-FTIR spectroscopy allows collection of infrared spectra from spots with ~20 nm spatial resolution. These two techniques also require minimal sample preparation and are nondestructive to the studied samples, making them suitable techniques for studying precious extraterrestrial samples including those that will be returned to Earth by the Hayabusa2 (JAXA) and OSIRIS-REx (NASA) missions.

In this paper, we present results of our detailed multi-technique spectroscopic investigation on the Didim meteorite, following a "from large (cm) scale to small (nm) scale" approach. Our aim is to describe its mineralogy, present molecular functional groups, and composition of present clasts/lithologies with high resolution. The information obtained from this approach may also help us understand possible parent body processes that the meteorite may have been subjected to.

SAMPLE AND EXPERIMENTAL METHODS

Meteorite Sample

Using a band saw, we cut a small piece (~30 gr) of Didim from the innermost part of a large (~1.2 kg) sample. The fresh side of this piece was first measured as bulk at the Planetary Spectroscopy Laboratory of the German Aerospace Center using a biconical reflectance spectroscopy instrument. This sample was further prepared as a thick polished section for our spectroscopic and microscopic investigations. Following the completion of micro-Raman and nano-FTIR measurements, the surface of the sample was coated with Au (thickness of 15–20 nm) for collecting backscattered electron microscopy images (Fig. 1).

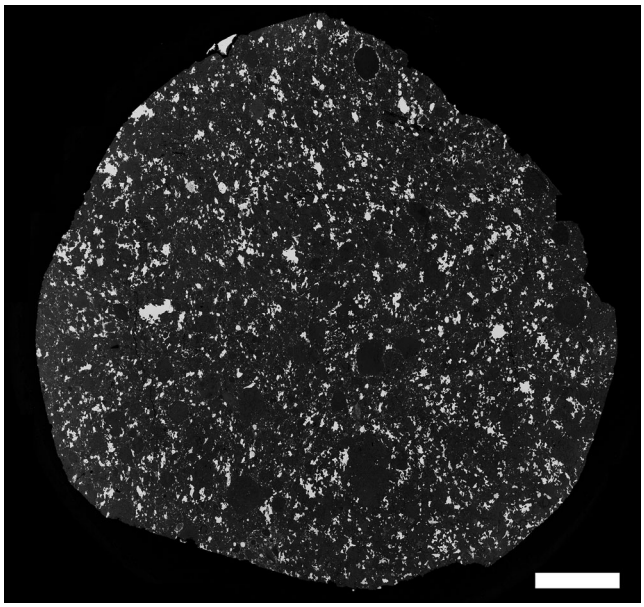

Fig. 1. Backscattered electron (BSE) mosaic image of the Didim meteorite showing overall texture of the sample. Image collected at an accelerating voltage of 15 kV and a beam current of 20 nA. White scale bar in the lower right is ~4 mm.

Experimental Methods

Biconical Reflectance Spectroscopy

We used two FTIR instruments (Bruker Vertex 80V) available in the Planetary Spectroscopy Laboratory (PSL) at DLR Berlin to measure biconical reflectance spectra of the thick Didim sample at variable incidence and emission angles. The spectrometers were evacuated to ~0.1 mbar and kept at this low pressure during the measurements. We used a GaP detector and a CaF_2 beam splitter with a deuterium lamp to cover the 0.2–0.5 μm (UV) range, an Si diode detector and a CaF_2 beam splitter and a water-cooled tungsten halogen lamp for the 0.4–1.1 μm (VIS) range, a nitrogen-cooled MCT (mercury cadmium telluride) detector along with a KBr beam splitter and a globar lamp for the 1–16 μm (VNIR + MIR) range, and a room temperature DTGS (deuterated triglycine sulfate) detector and Mylar multilayer beam splitter with a globar lamp to cover the

16–21 μm spectral range. The spectral resolution was 4 cm^{-1} for our measurements. A Bruker A513 accessory with a viewing cone aperture of 17° was used for our biconical reflectance measurements. VNIR spectra were normalized to spectralon while the rest of the spectral range was normalized to a gold reference (gold mirror). We measured three spectra for each set of angles for Didim, which were then averaged to generate a single spectrum for the specified angles.

Micro-Raman Spectroscopy

Micro-Raman spectroscopic measurements were conducted using a commercial confocal Raman imaging system (WiTec alpha300R) equipped with a 532 nm Nd: YAG laser and a 50× objective (NA = 0.8). Carbonaceous material and its structures can be artificially modified if high laser power is applied to the sample surface or when the sample is excited for long durations. A possible sign of the induced thermal alteration is the systematically shifting the peak parameters as a function of laser excitation (Busemann et al. 2007). The low laser power density on the sample surface (~0.57 to 0.85 mW μm^{-2}) and short integration times (0.3–0.5 s) of our measurements did not result in the systematically shifting spectral parameters (such as the width or the peak positions) when multiple laser shots were directed to the same spot, indicating no laser-induced modification of carbon structures. Two-dimensional Raman intensity maps of the surface were collected from various areas with a 0.5 μm step size (pixel size). In these 2-D images, every pixel within the measured area contains its own full Raman spectrum. For the 3-D tomography data set, following the methods of Yesiltas et al. (2018), we measured a particular region (40 × 40 μm^2 area) for a depth of 15 μm with 1 μm depth resolution, resulting in 15 two-dimensional datacubes. Intensity distribution maps of individual chemical components were generated by integrating the signal between the spectral endpoints of Raman peaks for each 2-D datacube. This procedure was repeated for each layer collected at different depths. The distribution maps of all layers were then imported to ImageJ software package, and all of the distribution maps were stacked individually, which were then imported to Avizo software package for visualization of the observed components in a 3-D space.

Nano-FTIR Spectroscopy

Principles and applications of nano-FTIR spectroscopy are presented elsewhere (e.g., Huth et al. 2012; Dominguez et al. 2014; Kebukawa et al. 2019). In summary, to obtain broadband spectral information, a standard metal-coated AFM-tip is illuminated by broadband infrared radiation, and the backscattered light with two properties (amplitude and phase) is analyzed with a Michelson interferometer-based FTIR spectrometer (Huth et al. 2012). Among the two properties, the phase spectra are connected with the local absorption of the investigated sample (Taubner et al. 2004; Stiegler et al. 2011); therefore, the phase spectra were presented here. Our nano-FTIR experiments were conducted on a commercial s-SNOM system (neaspec GmbH) equipped with a broadband DFG laser. Spectra were collected with 20 nm spatial and 4 cm^{-1} spectral resolution from selected areas at the surface of Didim within the 1600–850 cm^{-1} spectral range to investigate the peaks in the molecular fingerprint region and detect various functional groups. All AFM scans were done in non-contact mode using Arrow-NCPt cantilever (resonance frequency: 285 kHz, spring constant: 42 N m^{-1}). The collected infrared spectra were then normalized using a gold mirror standard.

RESULTS

Biconical Reflectance Spectroscopy

Reflectance spectroscopy of ordinary chondrites within the VNIR range generally contains two characteristic broad absorption bands (regime of volume scattering), Band I and Band II, which appear near 1 and 2 μm, respectively. The former band (Band I) is mainly due to olivine with some contribution from pyroxene (Gaffey et al. 1993; Mothé-Diniz et al. 2008; Sanchez et al. 2014), and appears as a result of transitions of Fe^{2+} in the M1 and M2 crystallographic sites (King and Ridley 1987; Burns 1993; Sunshine et al. 2007). The latter band (Band II) is due to pyroxene (Gaffey et al. 1993) and appears as a result of electronic transitions of Fe^{2+} in M2 crystallographic sites (Mothé-Diniz et al. 2008). Spectral properties such as band centers and areas of Band I and Band II have been studied to unravel the surface mineralogy of asteroids and chemical content of meteorites (e.g., Cloutis and Gaffey 1991; Klima et al. 2007; Sunshine et al. 2007; Mothé-Diniz et al. 2008; Reddy et al. 2015). For instance, the area ratio of Band I and Band II was used to determine the olivine-to-orthopyroxene ratio for olivine–orthopyroxene mixtures, and also to differentiate different ordinary chondrite types (Gaffey et al. 1993). Furthermore, asteroids have been grouped into different classes based on their VNIR reflectance spectra (Bus and Binzel 2002; DeMeo et al. 2009), and visible-infrared spectral parameters of meteorites were compared with those of asteroids (Hiroi et al. 2010) for parent body identification purposes.

We measured biconical reflectance spectra of a bulk sample of Didim between 0.3 and 21 μm at three

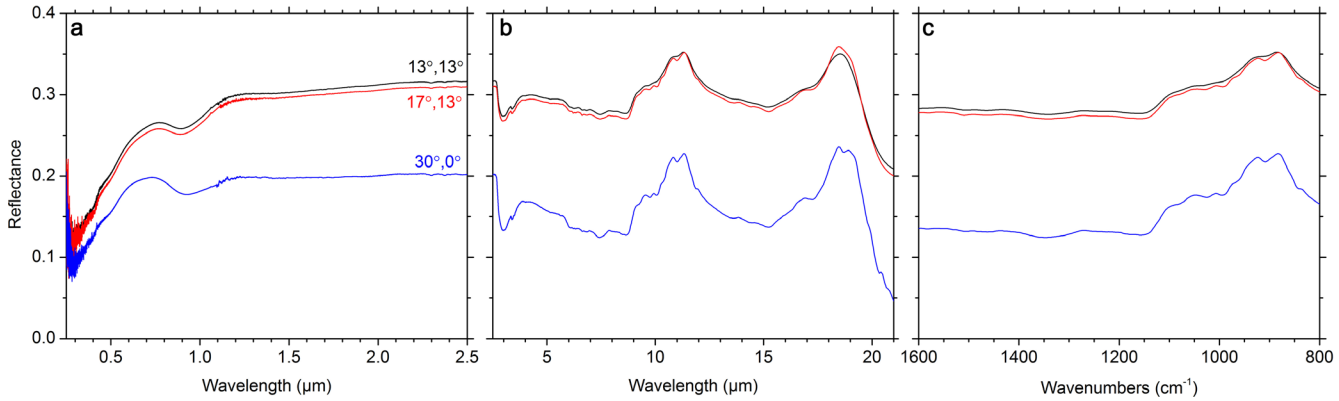

Fig. 2. Biconical reflectance spectra of Didim between 0.3 and 25 μm at three different orientations with incidence and emergence angles at *ie* = 13°:13°, 17°:13°, and 30°:0° (a, b). For these measurements, the aperture was ~ 3 mm, which means the field of view on the sample was no larger than 5 mm. The mid-infrared region (1600–800 cm^{-1}) is additionally shown in wave numbers scale in (c). (Color figure can be viewed at wileyonlinelibrary.com.)

different orientations with incidence (*i*) and emergence (*e*) angles at *i*:*e* = 13°:13°, 17°:13°, and 30°:0° (Fig. 2a). The respective phase angles for these measurements were 26°, 30°, and 30°, with 0° azimuth angle. The VNIR spectra for all three angle sets contain a broad band centered near ~0.93 μm. This position is at a shorter wavelength than generally observed Band I position (~1 μm), indicating the presence of a substantial amount of a different optically active minerals such as low-Ca pyroxene or possibly hematite in Didim. The rest of the spectra are relatively flat with only a weakly pronounced broad band near ~1.75 μm. Such a weak band could be due to several reasons. The absence of abundant pyroxene may diminish the depth of this band, or the sample type could possibly affect this band (slab versus particulate). Some of the slab ordinary chondrites in the RELAB database show a similar weak band near this position. Therefore, the flat surface of the sample might be particularly suppressing this band. Based on the VNIR spectra of Didim collected at *i*,*e* = 30,0°, the Band II/Band I area ratio is calculated to be ~0.30. We chose *i*,*e* = 30,0° to calculate the band area because the spectrum of this angle set requires the minimum baseline correction. Comparing the spectral band parameters with the parameters reported in the literature (e.g., Fieber-Beyer et al. 2012; Sanchez et al. 2014), we find that the VNIR spectral parameters of Didim are very similar to samples that contain olivine+orthopyroxene mixtures, and it falls very close to the H type ordinary chondrite region. These results are in agreement with the classification of this meteorite. We note that the band area ratios extracted from the VNIR spectra may not be a good indicator for the olivine content when non-particulate samples, such as Didim, are studied. Band shapes and positions should also be carefully assessed.

The longer wavelength part of the reflectance spectra (mid- and far-infrared region) present peaks (regime of surface scattering) mainly near the 9–12 μm and 18–21 μm regions, which are due to Si-O stretching and bending vibrations in silicates in the sample (Fig. 2b). Specifically, the 9–12 μm region is dominated by olivine peaks, possibly with some contribution from pyroxene. The doublet near 11.2 μm with weak features near 10 μm can be attributed to olivine. The 18–21 μm region presents peaks due to combination of olivine and pyroxene. The IR spectra are mostly similar for all three angle sets, but spectral differences do exist. For instance, there is a trend for the peak near 18.7 μm. This peak in the $i = 13°$ spectrum is rounded and symmetrical; however, the $i = 17°$ spectrum has an asymmetric peak with a less developed feature at 19.04 μm. This doublet is then fully developed for the $i = 30°$ spectrum. Overall, our VIS-IR reflectance spectra show that Didim contains anhydrous silicates, mainly olivine with some contribution from pyroxene. The peak at 3 μm (due to O-H stretching modes in water) and small features near 3.4 μm (due to aliphatic C-H stretching modes) are probably terrestrial contamination. It is worth noting that the strength of the 3 μm feature is the strongest for the spectrum with the smallest Fresnel contribution (30°, 0°), suggesting these features might now be an inherent part of the meteorite itself. The mid-infrared spectra are also shown in wave numbers (cm^{-1}) scale in Fig. 2c to allow future comparisons across the different scale of measurements.

Micro-Raman Spectroscopy

We collected micro-Raman spectral imaging data from two locations on Didim (Locations I and II). Fig. 3a and 3b present visible light image of Location I,

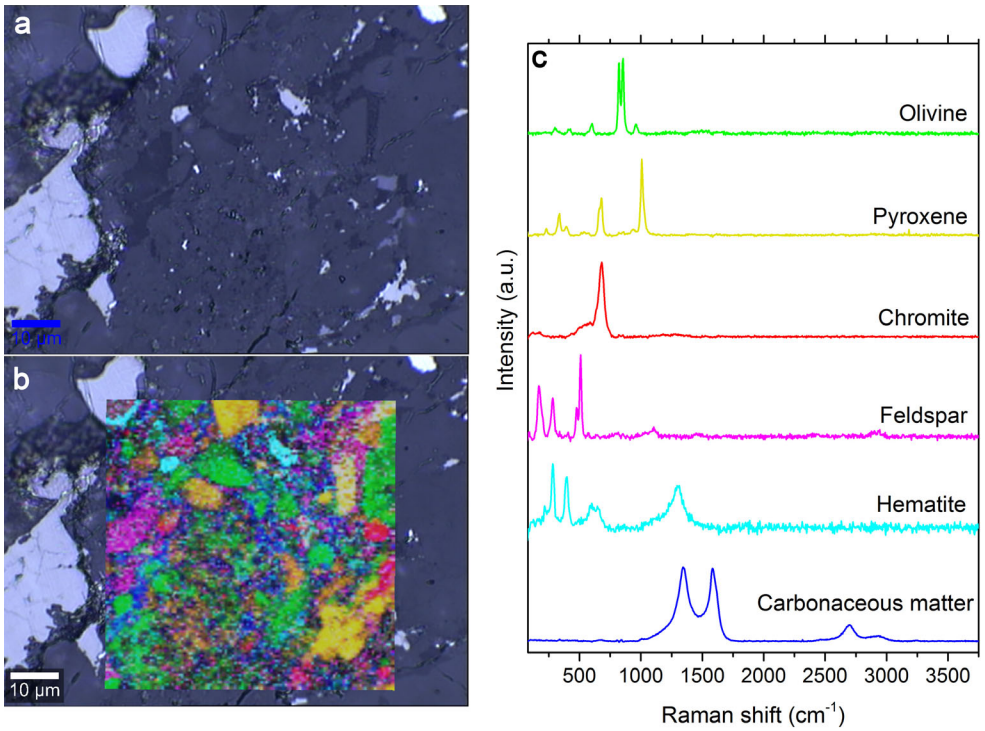

Fig. 3. Images and spectra of location I. a–b): Visible light image (top) and false-color chemical distribution map overlaid on the visible light image (bottom). Each color in the bottom image represents an individual chemical phase, whose corresponding Raman spectrum is shown in (c). (Color figure can be viewed at wileyonlinelibrary.com.)

where an area of 60 × 60 μm^2 was scanned. The false-color image contains various molecular phases, whose corresponding Raman spectra are shown in the right panel (Fig. 3-c). Olivine, pyroxene, feldspars, and opaque phases have been identified via their characteristic Raman peak positions and profiles.

Didim contains abundant olivine, evident from the strong doublet peak near 820 and 853 cm^{-1}. We calculated the Fo composition of olivine in Didim following the procedure described in Kuebler et al. (2006). Namely, using this doublet Raman peak and a pair of Lorentzian bands, we performed a fitting procedure to extract spectral parameters (spectral positions) of the two individual peaks from 85 pixels within an olivine-rich location. Our calculation yields that the Fo composition of Didim varies between Fo70 and Fo100 with average composition of Fo90 (Fig. S1 in supporting information), indicating the presence of a highly forsteritic (Mg-rich) mineralogy in some of the clasts of Didim. These Fo ranges are in agreement with the preliminary results of Didim (Fo80-Fo81 in the H5 lithology and Fo67-Fo100 in the H3 lithology) reported in the Meteoritical Bulletin.

Pyroxene is present in Didim as well, with characteristic Raman peaks at 330, 395, 671, and 1010 cm^{-1}. Clino- versus orthopyroxenes can be distinguished based on their Raman peaks and spectral profiles. Clinopyroxene presents a doublet with peaks at 332 and 390 cm^{-1} and two singlets near 668 and 1010 cm^{-1} (Huang et al. 2000; Wang et al. 2001). Orthopyroxene is characterized by a singlet near 332 cm^{-1}, a doublet at 658 and 678 cm^{-1}, and a singlet near 1006 cm^{-1} (Huang et al. 2000; Wang et al. 2001). These positions may vary with varying Fe, Mg, and/or Ca content of the phase. Our Raman measurements indicate that Didim contains both clino- and orthopyroxene phases. Figure 4 presents spatial distribution of these different types of pyroxenes as well as their corresponding Raman spectra observed in location I. Comparing with the RRUFF database (Lafuente et al. 2014), we see that clinopyroxene and orthopyroxene in Didim match best with augite and enstatite, respectively. Furthermore, the Mg^{2+} molar ratio in pyroxenes is estimated as 0.70–0.92 (n = 27 spectra) using the positions of the 330 and 671 cm^{-1} peaks and the calibration by Wang et al. (2001). These results are consistent with pyroxenes being augite and enstatite.

Carbonaceous material is observed in a few locations such as in the fine-grained matrix, and near the rims of some chondrules in Didim. Micro-Raman spectroscopy provides important information about the

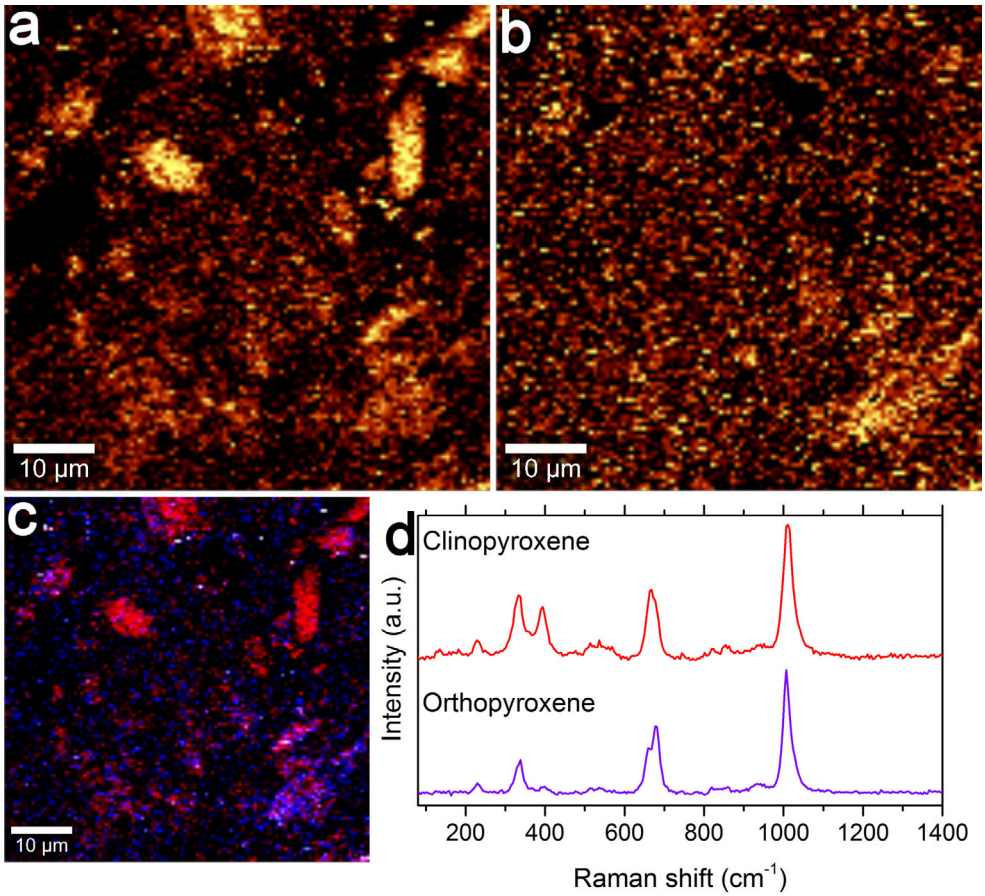

Fig. 4. Top: Raman intensity distribution maps of clinopyroxene (a) and orthopyroxene (b) observed in location I. Bottom: False-color distribution map of (a, red) and (b, blue) is shown in (c). Panel (d) presents corresponding Raman spectra. (Color figure can be viewed at wileyonlinelibrary.com.)

composition and structure of the carbonaceous material. Typically, the first-order carbon peaks appear near 1340 and 1590 cm^{-1}, and are known, respectively, as D ("defects") and G ("graphite") bands. Figure 5 presents, for Location I, carbon distribution maps of the D and G bands (panels a and b, respectively) and corresponding Raman spectra. Based on this distribution map, we observe that Didim contains both "disordered" (although less disordered than amorphous carbon) as well as "graphitic" (aromatic units are large, but still far from graphite) carbonaceous materials (Fig. 5c). Their corresponding Raman spectra are shown in Fig. 5d. A Lorentzian fitting procedure reveals additional bands within this first-order region. These bands are due to disordered carbon structures (D1, D2, D3, and D4 bands) and graphitic lattice vibrational modes (G band; Sadezky et al. 2005; Busemann et al. 2007; Brunetto et al. 2009; Suzuki et al. 2010). Specifically, the D1 band (due to disordered graphitic lattice, graphene layer edges) appears as a strong peak at 1348 cm^{-1}, the D2 band (related to disordered graphitic lattice) is a sharp feature near 1618 cm^{-1}, the D3 band (related to amorphous carbon) is a broad and weak peak near 1490 cm^{-1}, and the D4 band (due to disordered graphitic lattice) is a broad and weak feature around 1200–1250 cm^{-1} (Sadezky et al. 2005; Brunetto et al. 2009). The G band is attributed to graphitic lattice vibration modes in the polyaromatic carbon structures (Sadezky et al. 2005; Brunetto et al. 2009).

Intensity ratios of the D1 and G bands (I_D/I_G) are a relevant parameter in describing the length and size of the polyaromatic carbonaceous domains (Robertson 1986; Ferrari and Robertson 2000). We checked the I_D/I_G ratio of 100 carbon-rich pixels and observed that the average I_D/I_G ratio is ~1.2 (Fig. S1). This corresponds to a moderate degree of maturity for the carbon and small-to-medium size polyaromatic carbonaceous domains. The second-order carbon bands appear as a series of peaks with positions 2450, 2694, 2936, and 3237 cm^{-1} (Fig. 5). These peaks are combinations and overtones of the first-order carbon peaks (Sadezky et al. 2005; Brunetto et al. 2009). They are not always present

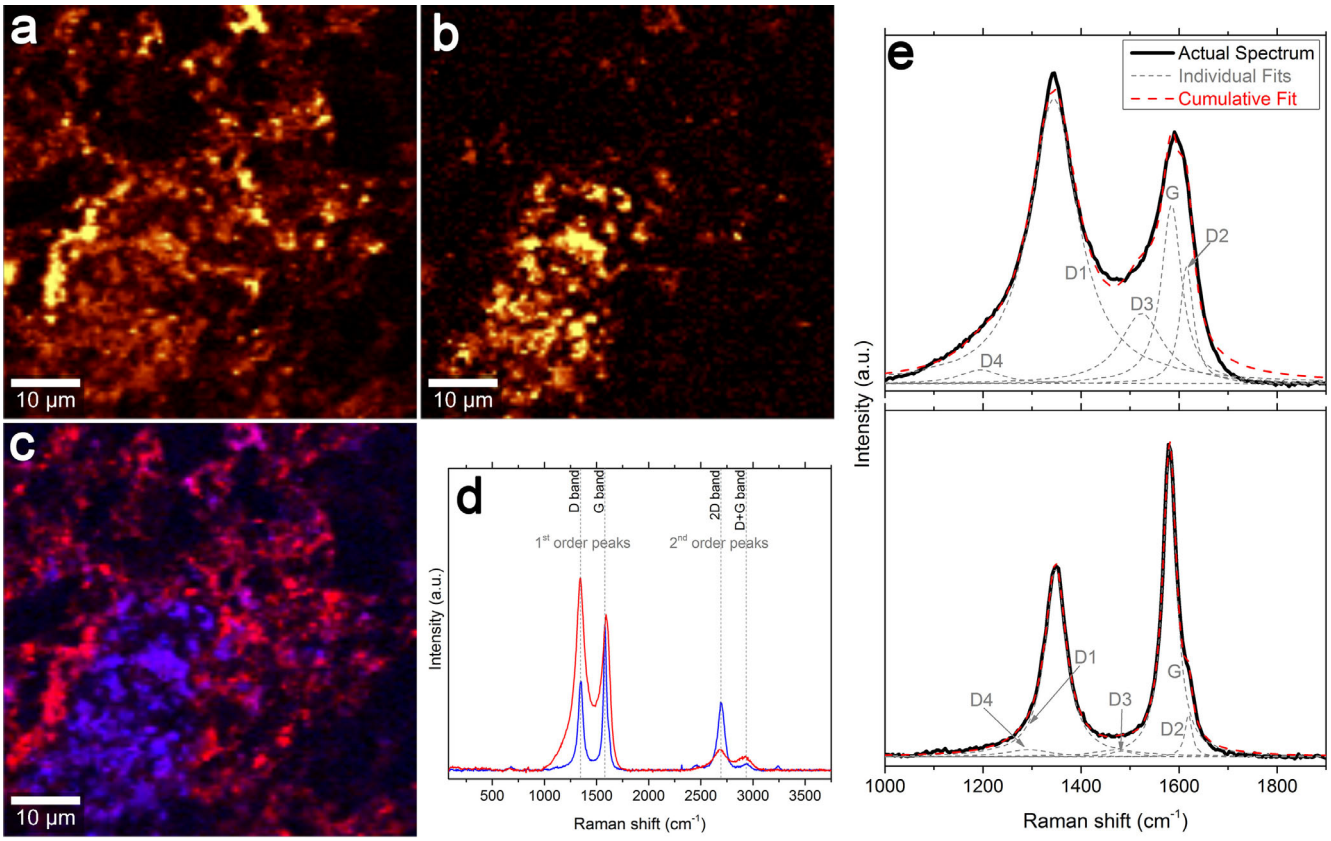

Fig. 5. Raman intensity distribution maps of first-order carbon D (a) and G (b) bands in the matrix of Didim. c: Their false-color combined distribution map (a: red, b:blue). d-e) Corresponding Raman spectra and first-order carbon peaks with their fitted curves, which reveal D1–D4 as well as G peaks. (Color figure can be viewed at wileyonlinelibrary.com.)

Table 1. Spectral positions of the observed Raman peaks and their assignments.

Positions (cm^{-1})	Assignment
821, 852, 961	Olivine
228, 332, 358, 392, 670, 1011	Pyroxene
483–602, 680	Chromite
87, 172, 282, 477, 508	Feldspar
219, 282, 394, 555–694, 1300	Hematite
1345, 1585, 2450, 2694, 2936, 3237	Carbonaceous matter

in the Raman spectra; however, they do appear when graphitic material is present in the sample.

Feldspars (174, 283, 478, 508 cm^{-1}), opaque phases such as chromite (542 and 678 cm^{-1}), and hematite (285, 394, 625, and 1300 cm^{-1}) are also observed in Didim. Observed Raman peaks, their positions, and assignments are collected in Table 1.

Meteorites are highly susceptible to terrestrial contamination. There is a chance that carbonaceous matter may be picked up from the ground where it fell, or it may be introduced during the sample preparation in the laboratory. Petrographic section preparation procedures may easily contaminate meteorites. However, we argue that the carbonaceous matter seen in Didim in this work is likely to be extraterrestrial origin on the basis of the presence of carbon in the interior of the studied sample. Namely, upon observing carbonaceous matter on the surface of Didim in Location I, we searched for another location on the surface and found that near the rim of a barred-olivine chondrule (Location II), carbonaceous matter exists as a "vein" structure. Figure 6 presents a map of a thin channel of carbonaceous matter (blue) separating olivine structures (green). We performed a Raman tomographic measurement on this location (40 × 40×15 μm^3 volume) to observe whether the interior of the sample contains carbonaceous matter as well. Our 3-D Raman measurement results show that carbon in Didim exists not only on the surface of the section but also in the interior of the sample. For instance, carbonaceous matter in Location II appears not only on the surface of the sample but also underneath olivine going further down toward the interior (Fig. 7). Panels in Fig. 7 right particularly show the presence of carbon underneath

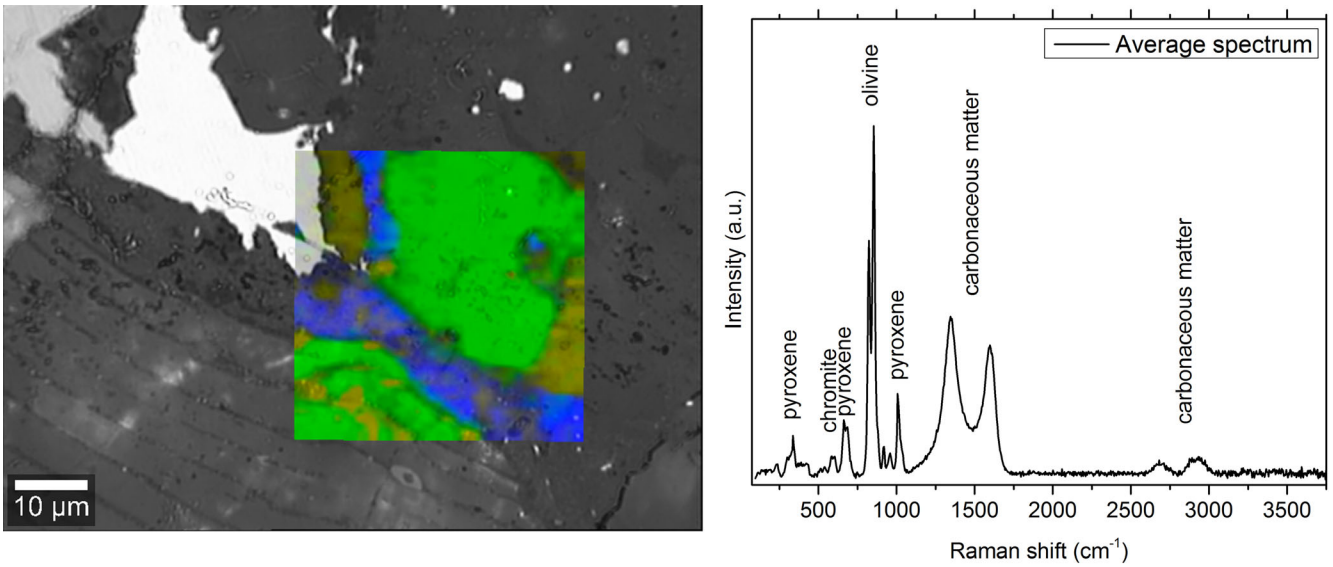

Fig. 6. Left) False-color chemical distribution map (green = olivine, yellow = pyroxene, blue = carbonaceous material) overlaid on visible light image of Location II. Right) Average Raman spectrum of this location. (Color figure can be viewed at wile yonlinelibrary.com.)

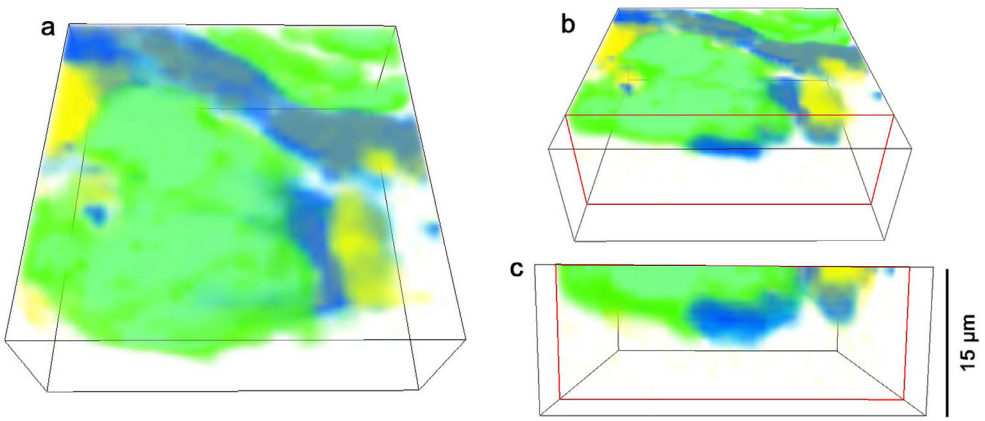

Fig. 7. a-c) 3-D distribution of chemical components observed in location II, given in different orientations (angles). Carbon is present in the interior of the meteorite, in addition to the surface. (Color figure can be viewed at wileyonlinelibrary.com.)

olivine, which is not detectable in the 2-D surface mapping measurement. The presence of carbon underneath olivine in the interior of the sample indicates that origin of the observed carbonaceous matter is likely extraterrestrial. We note that the spectral signatures (e.g., the profile of D and G bands) of the carbon underneath the olivine are similar to the spectral signature of the surface carbon.

Nano-FTIR Spectroscopy

We collected nano-FTIR spectra and AFM images from a number of locations on the surface of Didim in an effort to describe its chemical composition with higher spatial resolution. Figure 8 presents average nano-FTIR spectra of observed chemical components in Didim. Our results indicate that Didim contains abundant feldspars, olivine, pyroxene, and metal phases. Materials that we interpret as sulfates are also present in some regions, although this could be of terrestrial origin (see below).

Main feldspar peaks appear at 1161 and 1056 cm^{-1}, with smaller features at 1250, 1220, and 969 cm^{-1} (blue spectrum). Olivine spectrum contains two sharp peaks at 982 and 953 cm^{-1} (green spectrum). Pyroxene composition varies from region to region (orange spectra). The main peaks appear near 1091 and 977 cm^{-1}. Other features near 1153, 1016, and 933 cm^{-1} are present in some spectra but absent (or were not properly resolved) in others, possibly

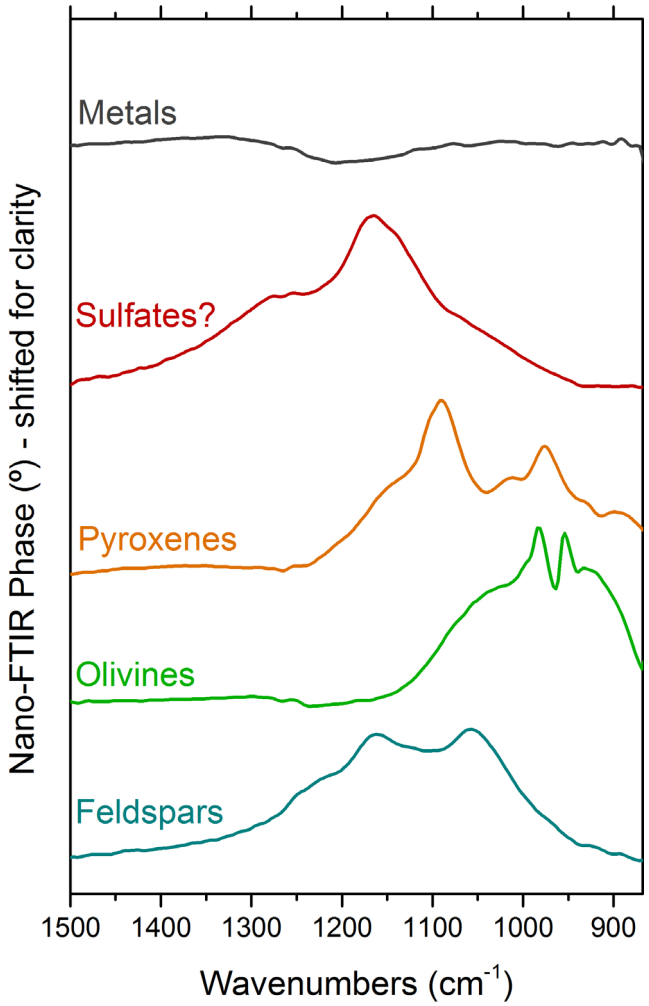

Fig. 8. Average nano-FTIR spectra of minerals and opaque phases observed in the Didim meteorite. (Color figure can be viewed at wileyonlinelibrary.com.)

indicating the presence of nano-scale molecular variations/heterogeneities in pyroxenes. The red spectrum presents two broad peaks centered near 1273 and 1164 cm^{-1}. These infrared bands fall within the range of sulfates (Gadsden 1975; Salisbury et al. 1991; Lane, 2007), therefore may be attributed to sulfates here, although this attribution is not unambiguous as the sulfates may be of terrestrial origin. These features may also be due to a glass component, such as silica glass; however, glassy materials have infrared peaks at slightly smaller wave numbers (at 1120 cm^{-1} versus 1150 cm^{-1}). Metal phases have a rather flat spectrum with no apparent feature (gray spectrum).

Using nano-FTIR spectroscopy, we investigated a total of six locations in Didim (different locations than Raman measurements). The presentation of our nano-FTIR is as follows: in Figs. 9 and 10 (and in Figs. S4–S7 in supporting information), we present visible light images of the investigated locations. Spots from where nano-FTIR spectra were collected within these locations are enumerated and marked with red circles in the visible light images. In some cases, multiple nano-FTIR spectra from much smaller materials were collected within these circled spots, which revealed spectrally distinct subregions. In these cases, an AFM image (images with gold color scale in Figs. 9 and 10, S4–S7) of the associated spot is provided with position indicators for the studied points. Among the six locations studied, results of the two locations (Locations III and IV) are reported in this manuscript, and results of the remaining locations are given in the associated supporting information document. Observed infrared peaks, their positions, and assignments are collected in Table 2.

Location III

Location III contains long veins, coarse-grained matrix material, and metallic phases (Fig. 9). Nano-FTIR spectra of the matrix material (spots 1, 2, 4, and 5 in Figs. 9a and 9c) have a distinct spectral profile, with peaks at 982, 955, and 921 cm^{-1}, which is consistent with olivine. Variations exist among the olivine spectra (see Discussion section), indicating the presence of compositionally heterogeneous olivine (possibly due to different Mg:Fe ratios), or, alternatively, the effects of spectral anisotropy in the matrix of Didim. Spot 3 is a vein that appears to be composed of fine-grained material. The AFM image of this spot (Fig. 9b) shows several particles with a lateral size of approximately 150 nm, whose nano-FTIR spectra present two major peaks at around 1165 and 1055 cm^{-1}. The individual point spectra from this spot are almost identical, with peak shifts of ~20 cm^{-1}. Feldspars such as labradorite, orthoclase, and one of its high pressure polymorph sanidine have peaks within these regions (Salisbury et al. 1987), and thus, these two peaks with slightly different center positions may be attributed to feldspars. Similar to olivine, observed feldspars also present compositional differences, and this is reflected in their spectra (see Discussion section). Metal phases generally present flat infrared spectral profile due to inactive infrared vibrational modes. Spot 6 of Location III is consistent with being a metallic phase, which appears bright in the visible light image (Fig. 9a). Nano-FT-IR spectra of various other metal phases are given in Fig. S8 in supporting information.

Location IV

Nano-FTIR spectra from 10 spots were collected in Location IV. Spots 1 and 2 appear as fine-grained

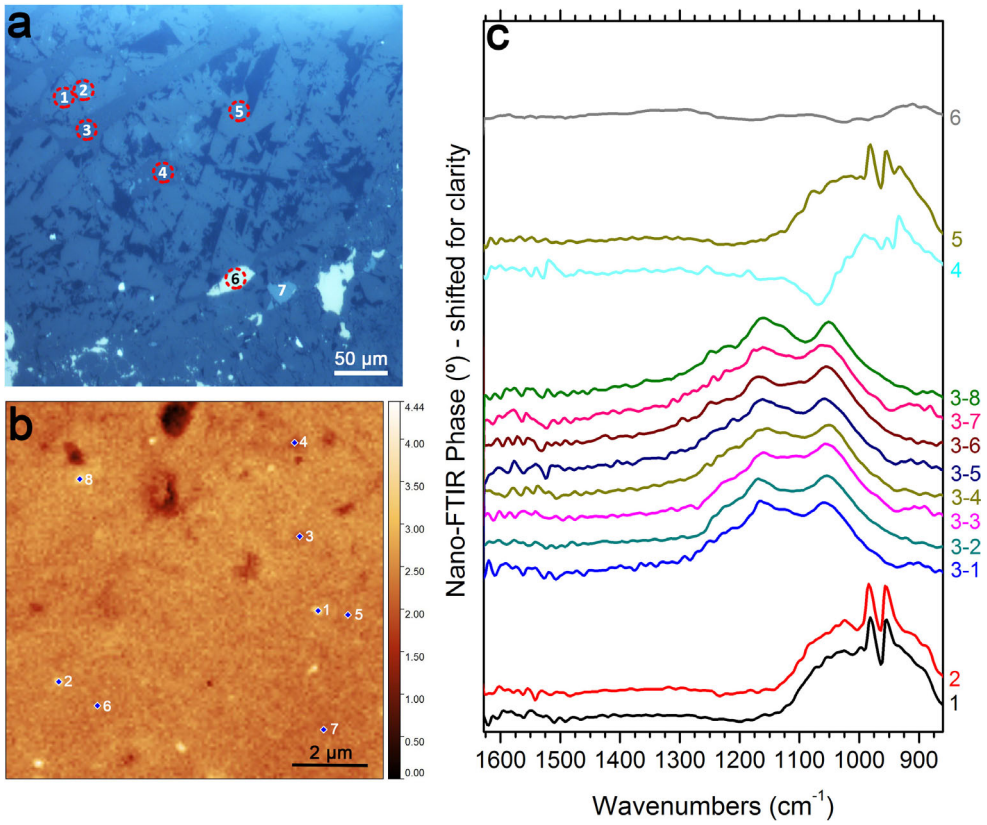

Fig. 9. a) Visible light image of Location III. The studied spots are indicated by a red dashed circle. b) AFM image of spot 3. Measured points in this spot are numbered from 1 to 8. c) Nano-FTIR spectra of corresponding spots and points. Olivine has a distinct spectra (such as spectra 1 and 2). Feldspar is characterized by two strong and a weak shoulder band (all spectra in spot 3). Spectrum 6 is due to an opaque metallic phase. (Color figure can be viewed at wileyonlinelibrary.com.)

material in Fig. 10a, and are further investigated via AFM images. Figure 10b shows the zoomed-in version of this fine-grained material. The AFM images of spots 1 and 2 are visually and spectrally very similar to each other. They contain many needle-like features and small particles embedded inside the fine-grained material (Figs. 10c and 10d). Nano-FTIR spectra of these needle-like features present peaks near 1090, 982, and 925 cm^{-1}. These spectral profiles and peak positions are consistent with pyroxene minerals (Martin et al. 2017). Furthermore, the small particles (e.g., points 1–5 and 1–10 in Fig. 10c) and the matrix material (e.g., points 1–4 and 1–9 in Fig. 10c) present similar nano-FTIR spectra with major bands at 1164 and 1070 cm^{-1}, which can be attributed to pyroxenes. These pyroxene peaks are relatively broader in the case of the latter material, indicating nano-scale compositional differences (possibly due to different Mg/Fe and Ca/[Mg + Fe] ratios). Observed infrared spectra also present a small bump beyond 1220 cm^{-1}, which could be due to sulfates. Variations in the nano-FT-IR spectral peak positions suggest the presence of mixtures of olivine and pyroxene in varying amounts in other spots and points.

DISCUSSION

Type 3 chondrites are the least altered and metamorphosed chondrites, and are relatively pristine samples (Scott and Krot 2014). In this type, mineralogy is generally unequilibrated and silicates are heterogeneous. Beyond type 3, however, samples are relatively equilibrated due to progressing thermal metamorphism (Kovach and Jones 2010). For instance, type 5 chondrites were thermally heated to 500–800 °C (Keil 2000), which resulted in the growth of feldspar, chromite, and phosphate grains (Scott and Krot 2014). The Didim meteorite was classified as H3-5 ordinary chondrite; it contains a mixture of H3 and H5 lithologies in the sample (Weisberg et al. 2008). This is a relatively rare case; there are only 77 H3-5 chondrites among 53,983 ordinary chondrites as of today (the Meteoritical Bulletin Database). Thus, Didim provides an important opportunity for mineralogical and compositional investigations.

Olivine and feldspar composition of Didim appears to differ from average H chondrites. The olivine composition of most H chondrites (especially petrologic types 4–6) is

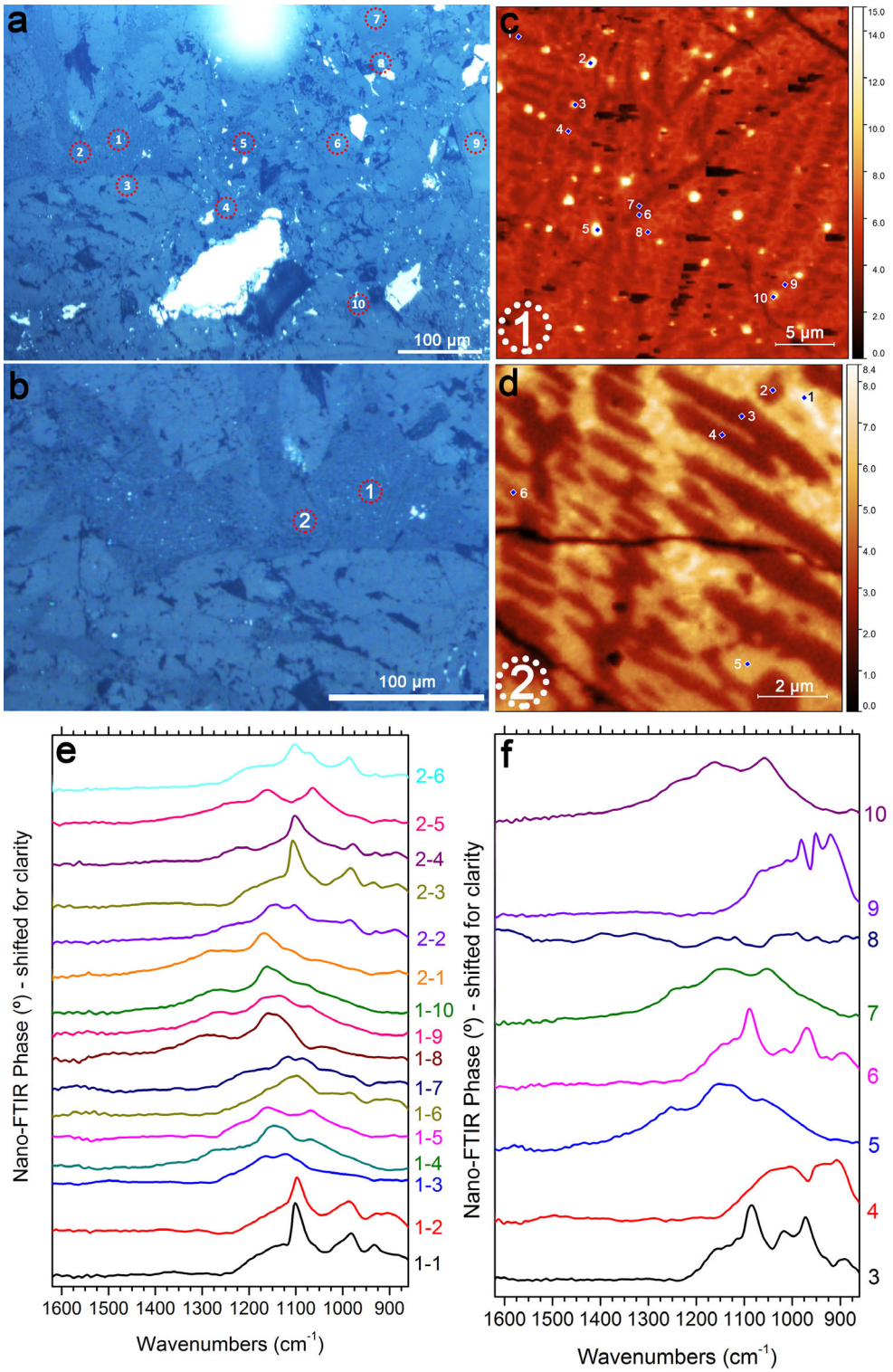

Fig. 10. a) Visible light image of Location IV. The studied spots are indicated by a red dashed circle. b) Close-up image of points 1 and 2. c, d) AFM images of spots 1 and 2. e, f) nano-FTIR spectra of corresponding spots and points. Spectra of spots 3 ad 6 present characteristic pyroxene bands. Spectra 5, 7, 10, 1–5, and 2–5 are due to feldspars. (Color figure can be viewed at wileyonlinelibrary.com.)

Table 2. Positions and assignments of observed infrared bands.

Wave number (cm^{-1})	Wavelength (μm)	Wave number (cm^{-1})	Wavelength (μm)
490*	20.40	991^{+}	10.09
503^{*O}	19.87	1012^{+S}	9.88
526*	19.00	1021^{+S}	9.79
540*	18.50	1030^{+S}	9.71
597*	16.75	1045^{+S}	9.57
637^{*P}	15.70	1055^{+P}	9.48
682*	14.66	1064^{+P}	9.40
720*	13.89	1081^{+}	9.25
837*	11.94	1086^{+}	9.21
863^{+PO}	11.59	1092^{+}	9.16
877^{+PO}	11.40	1104^{+}	9.06
883^{+O}	11.33	1121^{+S}	8.92
890^{+O}	11.24	1140^{+S}	8.77
896^{+O}	11.16	1145^{+}	8.73
901^{+}	11.10	1150^{+P}	8.70
906^{+}	11.04	1158^{+P}	8.64
917^{+P}	10.91	1165^{+}	8.58
925^{+PW}	10.81	1170^{+}	8.55
932^{+FaW}	10.73	1180^{+}	8.47
952^{+FoW}	10.50	1196^{+}	8.36
963^{+}	10.38	1225^{+}	8.16
972^{+}	10.29	1242^{+}	8.05
976^{+}	10.25	1254^{+}	7.97
982^{+}	10.18	1277^{+}	7.83
988^{+}	10.12		

*From FTIR reflectance spectroscopy; $^{+}$from nano-FTIR spectroscopy; ^{P}Pyroxene, ^{O}Olivine, ^{Fa}Fayalite, ^{Fo}Forsterite, ^{S}Silicates, ^{W}Absorbed water.

generally ~Fo80-Fo85 (Rubin 1990; Pittarello et al. 2015), whereas Didim contains more forsteritic olivine (~Fo70-Fo100). Such higher Fo content might be due to the contribution from relatively more heterogeneous olivine (i.e., Mg-rich) in type 3 clasts/lithologies, as olivine in types 4–6 is more or less homogeneous. Indeed, several other metamorphosed H chondrites with type 3 lithologies/clasts contain highly forsteritic composition as well. Examples include Acfer 343 (Fo74-Fo93), Dar al Gani 353 (Fo78-Fo94), and Dar al Gani 918 (Fo83-Fo98). In addition, the feldspar composition of H4-H6 chondrites is typically albitic (Brearley and Jones 1998; Kovach and Jones 2010). However, Raman spectra of feldspars in Didim are most similar to labradorite and anorthoclase, while nano-FTIR spectra are similar to labradorite, orthoclase, and sanidine. Thus, the studied feldspars in Didim appear less albitic in composition. Processes that could affect the feldspar composition are thermal metamorphism, aqueous alteration, shock metamorphism, and weathering. Feldspar composition can be heterogeneous in type 3 ordinary chondrites, and becomes relatively homogeneous in types 4–6 due to thermal metamorphism (Kovach and Jones 2010). This may suggest that the feldspar grains measured in this study might be from the H3 clast, which means sampling bias could also be the reason for our feldspar observations. In other words, only a limited number of feldspar grains were measured in this study and they may not be representative of the whole meteorite.

Terrestrial weathering is capable of altering the constituents of meteorites including the organic matter. In the case of Didim, we investigated pieces of a large (~1.2 kg) stone, which was kept inside a ziplock bag and stored inside a cabinet for many years. In an effort to minimize the effects of terrestrial weathering, the subject specimen of our work was freshly cut and removed from the innermost part of this large stone and subsequently investigated in the laboratory. Visual inspection revealed no sign of rust or oxidation on the extracted specimens. The FT-IR reflectance spectra shown in Fig. 2 of the thick slab show a broad band near 3 μm due to atmospheric water adsorbed by the sample. Heating the sample could substantially eliminate the adsorbed water; however, this step was not taken since the focus of current work did not involve Didim's water content. The FTIR reflectance spectra also show small features near 3.4 μm, which are due to C-H stretching vibrational modes of aliphatic hydrocarbons. This suggests that the thick slab must have picked up such contaminant organic material before the FTIR reflectance measurements, perhaps during the transportation or during the measurements where the sample was laid on three different flat sample stages. While these two components are present in the FTIR reflectance spectra of the thick slab, they are not present in the case of a smaller specimen that was studied via micro-Raman and nano-FTIR spectroscopy. Spectral features of aliphatic hydrocarbons (such as peaks within 1750–1250 cm^{-1}) are absent in the nano-FTIR spectra. Raman spectra of the carbonaceous material also do not show contaminant C-H peaks (Fig. S3 in supporting information).

In Didim, we have identified potentially indigenous carbonaceous matter via Raman imaging experiments. As a precaution and to avoid possible surface contaminants, we have also collected Raman spectra from the interior of the sample and located carbonaceous material about several micrometers below a large olivine grain. Raman spectra of this organic material do not show the contaminant C-H peaks within the 2800–3100 cm^{-1} region. Terrestrial weathering can also alter the organic content of meteorites by modifying the degree of ordering in carbon, which results in the modified D and G band parameters (i.e., decreased D and G bandwidths as well as increased I_D/I_G ratios; Busemann et al. 2007). This is

not the case for Didim. Its carbon peak parameters plot within the primitive chondrites (Fig. S2 in supporting information). These points suggest that the carbonaceous matter seen in Didim is likely of extraterrestrial origin.

It is not uncommon to identify carbon in ordinary chondrites. For instance, the presence of carbonaceous matter and clasts in ordinary chondrites has previously been reported by numerous authors (e.g., Moore and Lewis 1967; Brearley 1990; Rubin et al. 2005; Yesiltas 2018). Carbonaceous clasts in chondrites may have been formed either in the solar nebula (Brearley 1990) or in the parent body through asteroidal processes (Rubin et al. 2005). It is also possible that chemical constituents including carbonaceous matter of different planetary objects could be mixed through collisions. In this context, the carbonaceous material in Didim might be exogenous, perhaps delivered to the parent body of Didim via collisions. Thus, compositional and structural investigation of the carbonaceous matter in Didim may help us constrain parent body processes such as impacts and associated bodies. In this context, a brief examination of chondrules in Didim through an electron microscope shows fractures in the chondrules, which could be associated with a possible impact event. This argument is consistent with the presence of (1) both H3 and H5 materials, and (2) fine- and coarse-grained materials together in Didim. Furthermore, even the most disordered carbon observed via Raman in Didim seems to be more ordered than typical carbon in cometary IDPs or primitive carbonaceous chondrites (e.g., Brunetto et al. 2011). This implies that even if exogenous, carbon in Didim must have undergone some heating processes in the parent body. The comparison of FWHM of the G band with its peak position shows that carbon in Didim falls between the CV3 and CO3 range, while the band position spans a wide range (Fig. S2). This suggests that carbon in Didim must have undergone processes, such as thermal metamorphism and amorphization (perhaps as a result of ion irradiation), possibly in the parent body. In any case, investigation of carbonaceous material in Didim certainly requires further work. While determining the exact amount of carbon and the potential sources in Didim require utilization of additional techniques, it is not the focus of this work and therefore not explored further here.

Meteoritic constituents can compositionally vary on scales smaller than a micrometer; however, materials that are smaller than ~1 μm are normally not accessible via conventional infrared techniques. Nano-FTIR spectroscopy provides a unique opportunity and capability to interrogate samples in great detail to deduce information about the present chemical functional groups, which may help us understand and constrain parent body processes they may have undergone. Thus, nano-FTIR spectroscopy is not only a very useful nondestructive technique but also a unique capability for the investigation of small precious samples, such as that are being returned from primitive asteroids by OSIRIS-REx and Hayabusa2 missions. In this work, we have shown that s-SNOM-based nano-FTIR spectroscopy is capable of providing infrared spectral identification of various minerals and metallic phases with ~20 nm spatial resolution. It allowed us to probe the local mineralogy of lithologies in Didim in great detail. Didim is a unique ordinary chondrite with bright color H5 type equilibrated material set in a dark color H3 type host material, as such composition of these lithologies present differences. By imaging the area of interest with an optical microscope and collecting high spatial resolution point spectra from different locations on the surface, we were able to resolve nano-scale spectroscopic differences in Didim through AFM images and spectral peak shifts. These differences can be possibly explained by mineralogical and compositional differences in the studied phases which are not detectable at larger scales. Compositionally different mineral endmembers were detected through the differences in their spectral profile and peak positions observed in our nano-FTIR experiments on Didim. In the case of pyroxenes, for instance, the peak near 1083 cm^{-1} becomes more prominent, more intense, and shifts to higher frequencies (from bottom to top spectra in Fig. 11c). Olivine composition appears to vary from point to point, this variation is easily seen in Fig. 11b. An additional peak forms near 934 cm^{-1} and gradually shifts to lower frequencies, while the sharp peak near 982 cm^{-1} becomes wider (from bottom to top) and shifts to ~988 cm^{-1}. Similarly, the peak at 951 cm^{-1} shifts to 956 cm^{-1} from bottom to top. These spectral variation in olivine roughly correspond to Fo_{81}-Fo_{100} (Mg:Fe = ~0.8–1.0; Hofmeister and Pitman 2007; Hamilton 2010). Didim also contains compositionally different feldspars. Nano-FTIR spectra of feldspars present a peak near 1069 cm^{-1} that shifts to 1044 cm^{-1} and becomes broader for different points within the feldspars (Fig. 11a). While this shift occurs, a shoulder peak near 1228 cm^{-1} forms and then becomes more prominent. The feature near 1120 cm^{-1} is present in some spectra but absent in others in the spectra of feldspars. These variations can be due to the presence of different cations, such as K, Na, and Ca, in the composition of feldspars. Sulfates in meteorites may be terrestrial contamination and require careful assignment in meteorites. During storage in a laboratory or when interacting with terrestrial hydration components such as atmospheric water, sulfates originally present in a meteorite may be dissolved and remobilized, or sulfides

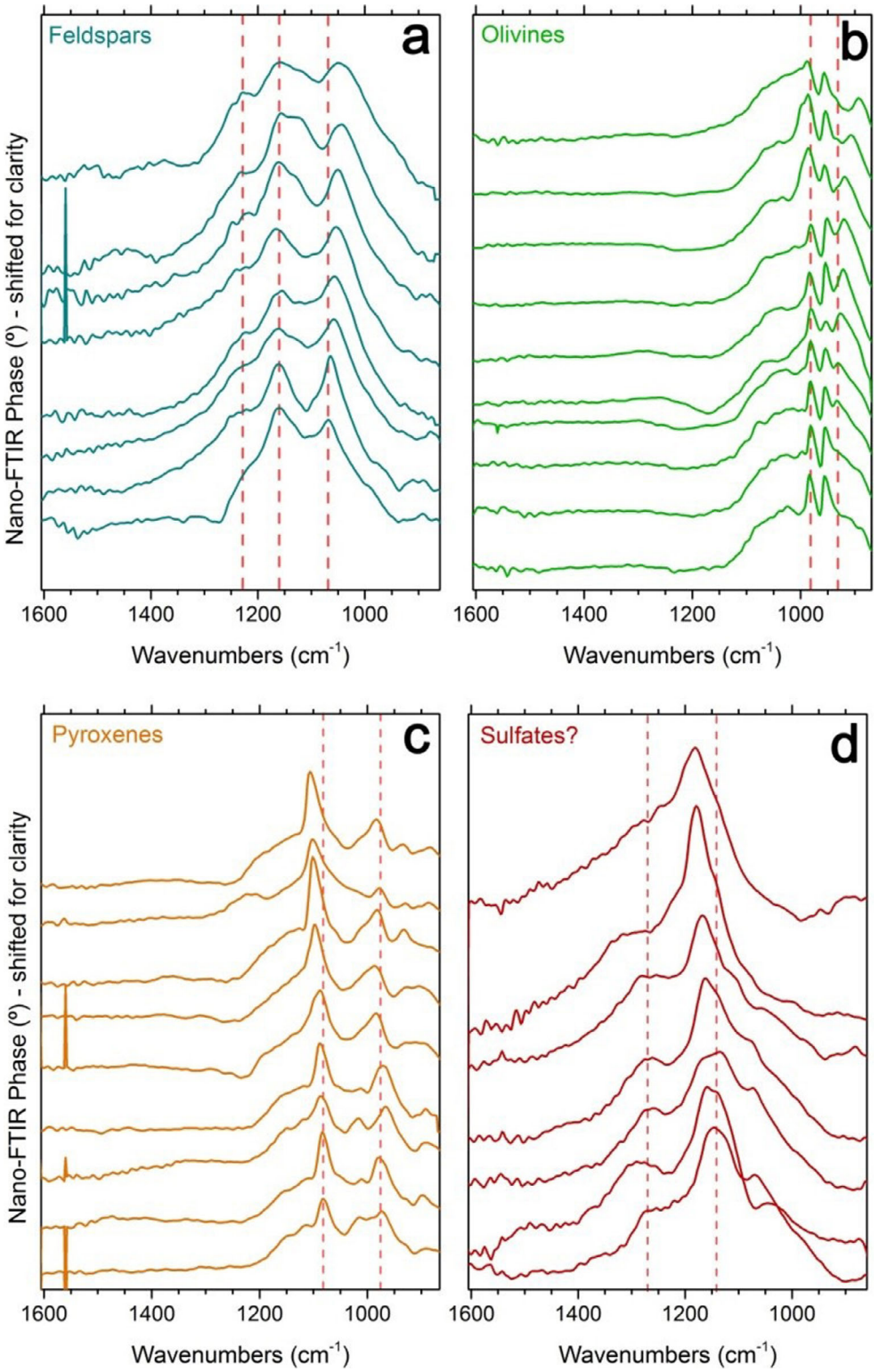

Fig. 11. Nano-scale spectral variations observed in Didim via nano-FTIR spectroscopy. a) Feldspars (blue), (b) olivines (green), (c) pyroxenes (orange), (d) sulfates (red). The very sharp feature near 1560 cm^{-1} is an artifact due to the noise captured in the infrared detector. Vertical dashed lines are shown for visual reference. (Color figure can be viewed at wileyonlinelibrary.com.)

may be oxidized and may fill open spaces and pores in the sample (Gounelle and Zolensky 2001). In Didim, several infrared bands appear beyond the silicate bands, and they are tentatively assigned as sulfates. However, we note that the sulfates seen here may be of terrestrial origin. In any case, the sulfates also show chemical/molecular variations even in 20 nm spatial distances. In the nano-FTIR spectra of Didim, the peak near 1143 cm^{-1} shifts to higher frequencies and becomes more prominent, while the small and broad peak near 1270 cm^{-1} disappears (from bottom to top spectra in Fig. 11d). The wave number difference for the peaks may be caused by the presence of different cations in sulfates. For instance, the presence of different cations such as Ca or Mg may shift the main broad peak to higher or lower frequencies (Lane 2007).

While the chemical variations and their infrared spectral signatures are easily captured for the Didim meteorite in this work, thanks to the nano-FTIR spectroscopy, we note that differences in crystal orientation may also contribute to the observed spectral differences. Namely, crystal orientation could cause spectral variability for any mineral that is not isotropic. In order to quantify its contribution and perform quantitative comparisons, extensive spectroscopic studies of mineral standards are needed.

CONCLUSIONS

Didim is a unique ordinary chondrite with both H3 and H5 lithologies even in a single stone. Its varied composition provides a unique opportunity to observe the chemical variations inside Didim with high resolution. Biconical reflectance spectroscopy of the bulk sample indicated the presence of olivine and some pyroxene in Didim, evident from the prominent band near 0.93 μm and very weak broad band near 1.75 μm crystal field band. Different incidence and emergence angle sets resulted in slightly different reflectance spectra for Didim. For instance, the peak near 19 μm is a singlet for $e = 13°$; however, this peak has more spectral features for $e = 30°$. The mid- and far-infrared regions present peaks mainly near the 9–12 μm and 18–20 μm regions due to Si-O stretching vibrations in silicates in the sample. The former region contains olivine bands (a doublet near 11.2 μm with weak features near 10 μm), while the latter region presents peaks due to combination of olivine and pyroxene. Our results show that Didim contains anhydrous silicates, mainly olivine and pyroxene, and some other optically active minerals.

Based on micro-Raman spectra, the Fo composition of olivine was estimated as Fo70-Fo100 with average composition of Fo90, and the Mg^{2+} molar ratio of pyroxene was estimated as 0.70–0.92. Carbonaceous matter was observed to be present in Didim as well. With an average I_D/I_G ratio, carbon in Didim experienced moderate degree of maturity and indicates the presence of small to- medium size polyaromatic carbonaceous domains. The presence of the second-order carbon bands indicates the presence of graphitic material in the sample. By performing a 3-D tomographic measurement, we showed that the carbonaceous matter is present not only on the surface but is also in the interior of the meteorite. Carbonaceous matter is also found underneath a large olivine grain, indicating that the carbonaceous materials observed in Didim are likely extraterrestrial in origin. Such carbonaceous material may have been delivered to the parent body of Didim via impacts/collisions. Our nano-FTIR spectroscopic investigation revealed that the mineralogy of Didim varies compositionally in scales smaller than a micrometer. For instance, nano-FTIR spectra of feldspars, olivine, pyroxene, and sulfates vary from point to point. Characteristic peak shifts to higher or lower wave numbers in the nano-FTIR spectra indicate the presence of compositionally different mineral endmembers.

Acknowledgments—We thank Istanbul Technical University staff members for preparing the thick meteorite sample for measurements. Members of the Planetary Spectroscopy Laboratory (DLR) are thanked for their assistance with reflectance experiments. We thank the Associate Editor and the anonymous reviewers for their constructive reviews and comments, which significantly improved this manuscript. Melissa D. Lane is also thanked for insightful discussions. We gratefully acknowledge support from TUBITAK (PI: M. Yesiltas), and EuroPlanet2020RI (PI: M. Yesiltas), which received funding from the European Union's Horizon 2020 research and innovation programme under grant agreement no 654208. This work was also supported by the RISE2 node of NASA's Solar System Exploration Research Virtual Institute (SSERVI; PI: T.D. Glotch). M.K. acknowledges the TARLA project, founded by the Ministry of Development of Turkey (project code: DPT2006K12-827). R.B. acknowledges support by the Centre National d'Etudes Spatiales (CNES-France, Hayabusa2 mission). The data presented here will be made publicly available at Turkish Spectral Database upon publication (http://tsd.klu.edu.tr).

Editorial Handling—Dr. Carlé Pieters

REFERENCES

Brearley A. J. 1990. Carbon-rich aggregates in type 3 ordinary chondrites: Characterization, origins, and thermal history. *Geochimica et Cosmochimica Acta* 54:831–850.

Brearley A. J. and Jones R. H. 1998. Chondritic meteorites. In *Planetary materials, reviews in mineralogy*, edited by Papike J. J. Washington, D.C.: Mineralogical Society of America. pp. 3–1–3-398.

Brunetto R., Pino T., Dartois E., Cao A. T., d'Hendecourt L., Strazzulla G., and Bréchignac P. 2009. Comparison of the Raman spectra of ion irradiated soot and collected extraterrestrial carbon. *Icarus* 200:323–337.

Brunetto R., Borg J., Dartois E., Rietmeijer F. J. M., Grossemy F., Sandt C., d'Hendecourt L. L. S., Rotundi A., Dumas P., Djouadi Z., and Jamme F. 2011. Mid-IR, Far-IR, Raman micro-spectroscopy, and FESEM–EDX study of IDP L2021C5: Clues to its origin. *Icarus* 212:896–910.

Burns R. G. 1993. *Mineralogical applications of crystal field theory*. New York: Cambridge University Press.

Bus S. J. and Binzel R. P. 2002. Phase II of the small main-belt asteroid spectroscopic survey: The observations. *Icarus* 158:106–145.

Busemann H., Alexander C. M. O'D., and Nittler L. R. 2007. Characterization of insoluble organic matter in primitive meteorites by microRaman spectroscopy. *Meteoritics & Planetary Science* 42:1387–1416.

Cloutis E. A. and Gaffey M. J. 1991. Pyroxene spectroscopy revisited: Spectral-compositional correlations and relationship to geothermometry. *Journal of Geophysical Research: Planets* 96(E5):22809–22826.

DeMeo F. E., Binzel R. P., Slivan S. M., and Bus S. J. 2009. An extension of the Bus asteroid taxonomy into the near-infrared. *Icarus* 202:160–180.

Dominguez G., Mcleod A. S., Gainsforth Z., Kelly P., Bechtel H. A., Keilmann F., Westphal A., Thiemens M., and Basov D. N. 2014. Nanoscale infrared spectroscopy as a non-destructive probe of extraterrestrial samples. *Nature Communications* 5:1–10.

Ferrari A. C. and Robertson J. 2000. Interpretation of Raman spectra of disordered and amorphous carbon. *Physical Review B* 61:14095.

Fieber-Beyer S. K., Gaffey M. J., Hardersen P. S., and Reddy V. 2012. Near-infrared spectroscopy of 3: 1 Kirkwood gap asteroids: Mineralogical diversity and plausible meteorite parent bodies. *Icarus* 221:593–602.

Fries M. and Steele A. 2008. Graphite whiskers in CV3 meteorites. *Science* 320:91–93.

Gadsden J. A. 1975. *The infrared spectra of minerals and related inorganic compounds*. Mineralogical Magazine, London: Butterworths. 277 p.

Gaffey M. J., Bell J. F., Brown R. H., Burbine T. H., Piatek J. L., Reed K. L., and Chaky D. A. 1993. Mineralogical variations within the S-type asteroid class. *Icarus* 106:573–602.

Gounelle M. and Zolensky M. E. 2001. A terrestrial origin for sulfate veins in CI1 chondrites. *Meteoritics & Planetary Science* 36:1321–1329.

Hamilton V. E. 2010. Thermal infrared (vibrational) spectroscopy of Mg–Fe olivines: A review and applications to determining the composition of planetary surfaces. *Geochemistry* 70:7–33.

Hiroi T., Jenniskens P., Bishop J. L., Shatir T. S., Kudoda A. M., and Shaddad M. H. 2010. Bidirectional visible-NIR and biconical FT-IR reflectance spectra of Almahata Sitta meteorite samples. *Meteoritics & Planetary Science* 45:1836–1845.

Hofmeister A. M. and Pitman K. M. 2007. Evidence for kinks in structural and thermodynamic properties across the forsterite–fayalite binary from thin-film IR absorption spectra. *Physics and Chemistry of Minerals* 34:319–333.

Huang E., Chen C. H., Huang T., Lin E. H., and Xu J. A. 2000. Raman spectroscopic characteristics of Mg-Fe-Ca pyroxenes. *American Mineralogist* 85:473–479.

Huth F., Govyadinov A., Amarie S., Nuansing W., Keilmann F., and Hillenbrand R. 2012. Nano-FTIR absorption spectroscopy of molecular fingerprints at 20 nm spatial resolution. *Nano Letters* 12:3973–3978.

Jenniskens P., Fries M. D., Yin Q. Z., Zolensky M., Krot A. N., Sandford S. A., Sears D., Beauford R., Ebel D. S., Friedrich J. M., and Nagashima K. 2012. Radar-enabled recovery of the Sutter's Mill meteorite, a carbonaceous chondrite regolith breccia. *Science* 338:1583–1587.

Kallemeyn G. W., Rubin A. E., Wang D., and Wasson J. T. 1989. Ordinary chondrites: Bulk compositions, classification, lithophile-element fractionations and composition-petrographic type relationships. *Geochimica et Cosmochimica Acta* 53:2747–2767.

Kebukawa Y., Kobayashi H., Urayama N., Baden N., Kondo M., Zolensky M. E., and Kobayashi K. 2019. Nanoscale infrared imaging analysis of carbonaceous chondrites to understand organic-mineral interactions during aqueous alteration. *Proceedings of the National Academy of Sciences of the United States of America* 116:753–758.

Keil K. 2000. Thermal alteration of asteroids: Evidence from meteorites. *Planetary and Space Science* 48:887–903.

King T. V. and Ridley W. I. 1987. Relation of the spectroscopic reflectance of olivine to mineral chemistry and some remote sensing implications. *Journal of Geophysical Research: Solid Earth* 92:11457–11469.

Klima R. L., Pieters C. M., and Dyar M. D. 2007. Spectroscopy of synthetic Mg-Fe pyroxenes I: Spin-allowed and spin-forbidden crystal field bands in the visible and near-infrared. *Meteoritics & Planetary Science* 42:235–253.

Kohout T., Jenniskens P., Shaddad M. H., and Haloda J. 2010. Inhomogeneity of asteroid 2008 TC_3 (Almahata Sitta meteorites) revealed through magnetic susceptibility measurements. *Meteoritics & Planetary Science* 45:1778–1788.

Kovach H. A. and Jones R. H. 2010. Feldspar in type 4–6 ordinary chondrites: Metamorphic processing on the H and LL chondrite parent bodies. *Meteoritics & Planetary Science* 45:246–264.

Kuebler K. E., Jolliff B. L., Wang A., and Haskin L. A. 2006. Extracting olivine (Fo–Fa) compositions from Raman spectral peak positions. *Geochimica et Cosmochimica Acta* 70:6201–6222.

Lafuente B., Downs R. T., Yang H., and Stone N. 2014. The power of databases: The RRUFF project. In *Highlights in mineralogical crystallography*, edited by Armbruster T. and Danisi R. M. Berlin, Germany: W. De Gruyter. pp. 1–30.

Lane M. D. 2007. Mid-infrared emission spectroscopy of sulfate and sulfate-bearing minerals. *American Mineralogist* 92:1–18.

Martin D. J., Pernet-Fisher J. F., Joy K. H., Wogelius R. A., Morlok A., and Hiesinger H. 2017. Investigating the shock histories of lunar meteorites Miller Range 090034, 090070, and 090075 using petrography, geochemistry, and micro-FTIR spectroscopy. *Meteoritics & Planetary Science* 52:1103–1124.

McCoy T. J., Wadhwa M., and Keil K. 1999. New lithologies in the Zagami meteorite: Evidence for fractional

crystallization of a single magma unit on Mars. *Geochimica et Cosmochimica Acta* 63:1249–1262.
Moore C. B. and Lewis C. F. 1967. Total carbon content of ordinary chondrites. *Journal of Geophysical Research* 72:6289–6292.
Mothé-Diniz T., Carvano J. M., Bus S. J., Duffard R., and Burbine T. H. 2008. Mineralogical analysis of the Eos family from near-infrared spectra. *Icarus* 195:277–294.
Pittarello L., Baert K., Debaille V., and Claeys P. 2015. Screening and classification of ordinary chondrites by Raman spectroscopy. *Meteoritics & Planetary Science* 50:1718–1732.
Reddy V., Dunn T. L., Thomas C. A., Moskovitz N. A., and Burbine T. H. 2015. Mineralogy and surface composition of asteroids. *Asteroids IV* 43–63.
Robertson J. 1986. Amorphous carbon. *Advances in Physics* 35:317–374.
Rubin A. E. 1990. Kamacite and olivine in ordinary chondrites: Intergroup and intragroup relationships. *Geochimica et Cosmochimica Acta* 54:1217–1232.
Rubin A. E., Trigo-Rodriguez J. M., Kunihiro T., Kallemeyn G. W., and Wasson J. T. 2005. Carbon-rich chondritic clast PV1 from the Plainview H-chondrite regolith breccia: Formation from H3 chondrite material by possible cometary impact. *Geochimica et Cosmochimica Acta* 69:3419–3430.
Sadezky A., Muckenhuber H., Grothe H., Niessner R., and Pöschl U. 2005. Raman microspectroscopy of soot and related carbonaceous materials: spectral analysis and structural information. *Carbon* 43:1731–1742.
Salisbury J. W., Walter L. S., and Vergo N. 1987. Mid-infrared (2.1-25 um) spectra of minerals/(No. 87-263). Reston, Virginia: US Geological Survey.
Salisbury J. W., Walter L. S., Vergo N., and D'aria D. M. 1991. *Infrared (2.1-25 um) spectra of minerals*. Baltimore, Maryland: Johns Hopkins University Press. 9780801844232.
Sanchez J. A., Reddy V., Kelley M. S., Cloutis E. A., Bottke W. F., Nesvorný D., Lucas M. P., Hardersen P. S., Gaffey M. J., Abell P. A., and Le Corre L. 2014. Olivine-dominated asteroids: Mineralogy and origin. *Icarus* 228:288–300.
Scott E. R. D. and Krot A. N. 2014. Chondrites and their components. In *Meteorites and cosmochemical processes*, edited by Davis A. M. Treatise on Geochemistry, vol. 1. Amsterdam: Elsevier. 65–137.
Snape J. F., Joy K. H., and Crawford I. A. 2011. Characterization of multiple lithologies within the lunar feldspathic regolith breccia meteorite Northeast Africa 001. *Meteoritics & Planetary Science* 46:1288–1312.
Stiegler J. M., Abate Y., Cvitkovic A., Romanyuk Y. E., Huber A. J., Leone S. R., and Hillenbrand R. 2011. Nanoscale infrared absorption spectroscopy of individual nanoparticles enabled by scattering-type near-field microscopy. *ACS Nano* 5:6494–6499.
Sunshine J. M., Bus S. J., Corrigan C. M., McCoy T. J., and Burbine T. H. 2007. Olivine-dominated asteroids and meteorites: Distinguishing nebular and igneous histories. *Meteoritics & Planetary Science* 42:155–170.
Suzuki A., Yamanoi Y., Nakamura T., and Nakashima S. 2010. Micro-spectroscopic characterization of organic and hydrous components in weathered Antarctic micrometeorites. *Earth, Planets and Space* 62:33–46.
Taubner T., Hillenbrand R., and Keilmann F. 2004. Nanoscale polymer recognition by spectral signature in scattering infrared near-field microscopy. *Applied Physics Letters* 85:5064–5066.
Wang A., Jolliff B. L., and Haskin L. A. 1999. Raman spectroscopic characterization of a Martian SNC meteorite: Zagami. *Journal of Geophysical Research: Planets* 104:8509–8519.
Wang A., Jolliff B. L., Haskin L. A., Kuebler K. E., and Viskupic K. M. 2001. Characterization and comparison of structural and compositional features of planetary quadrilateral pyroxenes by Raman spectroscopy. *American Mineralogist* 86:790–806.
Weisberg M. K., Smith C., Benedix G., Folco L., Righter K., Zipfel J., Yamaguchi A., and Aoudjehane H. C. 2008. The Meteoritical Bulletin, No. 94. *Meteoritics & Planetary Science* 43: 1551–1584.
Yesiltas M. 2018. Investigation of carbon in the Allan Hills A77278 meteorite via 2D and 3D Raman microspectroscopy. *Journal of Raman Spectroscopy* 49:1812–1821.
Yesiltas M., Jaret S., Young J., Wright S. P., and Glotch T. D. 2018a. Three-dimensional raman tomographic microspectroscopy: A novel imaging technique. *Earth and Space Science* 5:380–392.
Yesiltas M., Glotch T. D., Jaret S., Verchovsky A. B., and Greenwood R. C. 2019. Carbonaceous matter in the Sariçiçek meteorite. *Meteoritics & Planetary Science* 54:1495–1511.
Yesiltas M., Young J., and Glotch T. D. 2020. Thermal metamorphic history of Antarctic CV3 and CO3 chondrites inferred from the first and second order Raman peaks of polyaromatic organic carbon. *American Mineralogist*. https://doi.org/10.2138/am-2021-7507.

SUPPORTING INFORMATION

Additional supporting information may be found in the online version of this article.

Fig. S1 Fo composition of olivine in Didim determined via Raman spectroscopy using the calibration expression and data in Kuebler et al. (2006).

Fig. S2 Left: Comparison of I_D/I_G ratios with full width half maxima values of the D band. CV3 and CO3 data are from Yesiltas et al. (2020).

Fig. S3 Comparison of carbonaceous matter in Didim (blue spectra) and the contaminant resin (red spectrum).

Fig. S4 (a) Visible light image of Location V. White scale bar is 100 μm. The studied spots are indicated by a red dashed circle. (b) AFM image of spot 3. (c) nano-FTIR spectra of corresponding spots and points.

Fig. S5 (a) Visible light image of Location VI. White scale bar is 100 μm. The studied spot is indicated by a red dashed circle. (b) AFM image of spot 1. (c) nano-FTIR spectra of corresponding spots and points.

Fig. S6 (a) Visible light image of Location VII. White scale bar is 100 μm. White scale bar is 100 μm. The studied spots are indicated by red dashed circles. (b) AFM image of spot 2. (c) Nano-FT-IR spectra of corresponding spots and points.

Fig. S7 (a) Visible light image of Location VIII. White scale bar is 100 μm. The studied spots are indicated by red dashed circles. (b,c) AFM images of spots 1 and 2. (d,e) nano-FT-IR spectra of corresponding spots and points.

Fig. S8 Nano-scale infrared spectral variations in metals.